Bringing nanomagnetism to the mesoscale with artificial amorphous structures

G. Muscas,[1,*] R. Brucas,[2] and P. E. Jönsson[1,†]

[1]*Department of Physics and Astronomy, Uppsala University, Box 516, SE-751 20 Uppsala, Sweden*

[2]*Department of Engineering Sciences, Uppsala University, Box 534, SE-751 21 Uppsala, Sweden*

(Received 21 February 2018; revised manuscript received 16 April 2018; published 9 May 2018)

In the quest for materials with emergent or improved properties, an effective route is to create artificial superstructures. Novel properties emerge from the coupling between the phases, but the strength of this coupling depends on the quality of the interfaces. Atomic control of crystalline interfaces is notoriously complicated and to elude that obstacle, we suggest here an all-amorphous design. Starting from a model amorphous iron alloy, we locally tune the magnetic behavior by creating boron-doped regions by means of ion implantation through a lithographic mask. This process preserves the amorphous environment, creating a non-topographic magnetic superstructure with smooth interfaces and no structural discontinuities. The absence of inhomogeneities acting as pinning centers for the magnetization reversal is demonstrated by the formation of magnetic vortexes for ferromagnetic disks as large as 20 μm in diameter embedded within a paramagnetic matrix. Rigid exchange coupling between two amorphous ferromagnetic phases in a microstructured sample is evidenced by an investigation involving first-order reversal curves. The sample consists of a soft matrix with embedded elements constituting a hard phase where the anisotropy originates from an elongated shape of the elements. We provide an intuitive explanation for the micrometer-range exchange coupling mechanism and discuss how to tailor the properties of all-amorphous superstructures.

DOI: 10.1103/PhysRevB.97.174409

I. INTRODUCTION

Technological progress is driven by our ability to manipulate material properties. Mixing two or more components in a single structure is an effective way to engineer materials with improved or emergent properties [1–4]. The control of the coupling between the components can be achieved by tailoring the periodicity, the sizes and shapes of the individual elements in the composite [5–7], as well as the quality of the interfaces [8–10]. Recent progress has been made in tuning these parameters both for two and three-dimensional superstructures [11–14]. Interfaces, however, are notoriously difficult to control; in particular the defects inevitably associated with crystalline interfaces such as dislocation and grain boundaries [15].

A way to avoid the problem of crystalline defects at structural interfaces is to use amorphous materials. Amorphous layers have been shown to give both smoother interfaces and improved performance compared with crystalline layers for spintronic applications [16–18]. In addition, layered amorphous structures have shown magnetic coupling phenomena and interface effects over much longer length scales than crystalline materials [19–21], and the physical properties of the individual layers can be tuned by finely adjusting their chemical composition during the thin-film deposition process [22–24]. To create superstructures with lateral "patterns," the lateral chemical composition also needs to be engineered. This is viable by using ion implantation combined with masking to locally dope the thin amorphous film. Focusing on magnetic materials, ion implantation and irradiation has so far been used to alter the magnetic properties by creating local disorder [25–30], to induce crystallization or stress in amorphous layers [31,32], and to locally change the chemical structure of crystalline phases [33–36].

To demonstrate the feasibility of creating amorphous magnetic superstructures using ion implantation and masking, we selected $Fe_{89}Zr_{11}$ as the target because it is a well-studied soft magnetic material [37,38], and its magnetic properties can be tuned continuously by controlling the chemical composition [24,37,39]. Doping it with, e.g., boron induces a small volume expansion, increasing the atomic Fe-Fe distance [40,41], which enhances the exchange coupling, as described by the Bethe–Slater curve [42]. The increased average exchange coupling gives a higher Curie temperature T_C and a reduction of the exchange frustration, resulting in lower coercivity [38,40]. In a previous study [38], we showed that implanting boron into an $Fe_{93}Zr_7$ film is feasible without creating additional surface roughness or crystallization of the target. Since the T_C of the $Fe_{89}Zr_{11}$ film is below room temperature (RT), we use temperature as a parameter to tailor the magnetic properties of the matrix from paramagnetic (PM) at RT to ferromagnetic (FM) at low temperature, while the B-implanted areas remain FM even at RT.

II. ALL-AMORPHOUS DESIGN

The fabrication of a fully amorphous superstructure consisting of B-implanted elements of various shapes embedded in a $Fe_{89}Zr_{11}$ matrix is schematically illustrated in Fig. 1. First, a 150 Å amorphous $Fe_{89}Zr_{11}$ thin film was deposited by using magnetron sputtering on an amorphous $Al_{70}Z_{r30}$ buffer

*giuseppe.muscas@physics.uu.se

†petra.jonsson@physics.uu.se

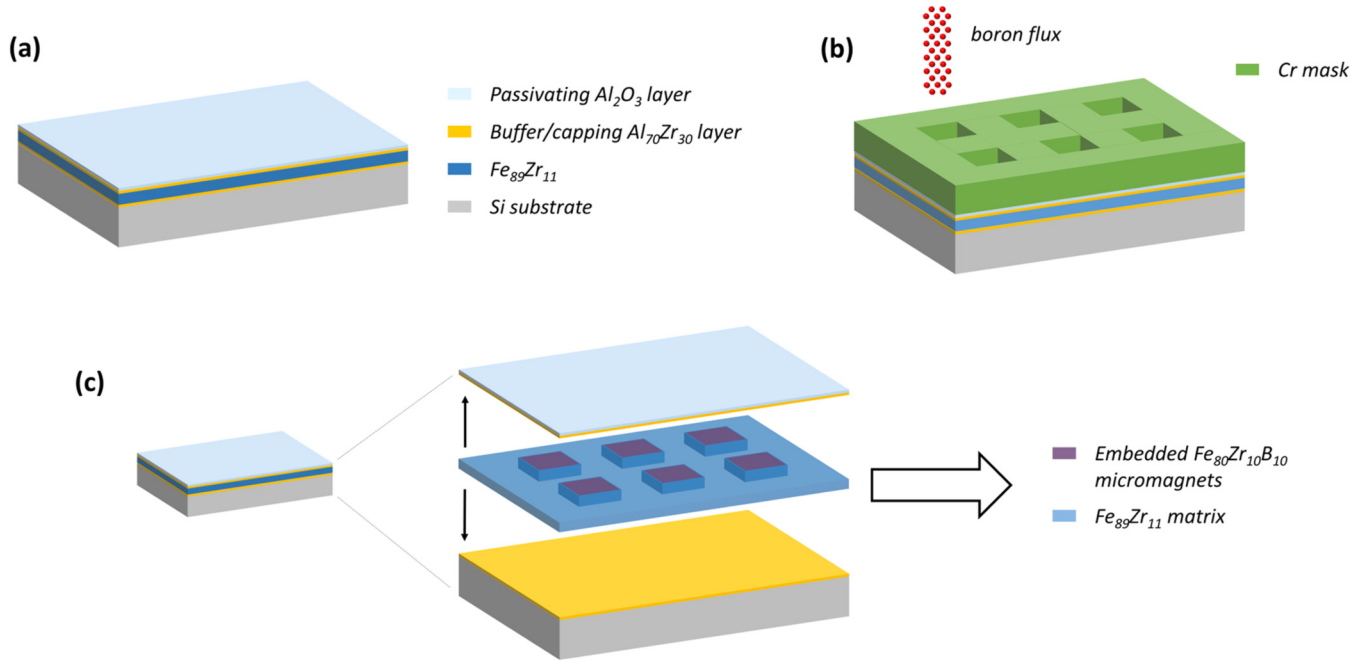

FIG. 1. (a) Schematic representation of multilayer structure of as-grown sample. (b) The desired pattern is reproduced on the sample with a Cr mask, then a boron-ion beam is scanned over the sample surface for implantation. (c) Finally, the mask is removed leaving the sample with its original layer structure with the addition of room-temperature ferromagnetic $Fe_{80}Zr_{10}B_{10}$ elements embedded in the paramagnetic $Fe_{89}Zr_{11}$ matrix.

layer [43]. The nominal composition of the $Fe_{89}Zr_{11}$ layer was verified by using Rutherford backscattering spectrometry (RBS), followed by the analysis of the spectra by using the simulation software SIMNRA [44], and found to lie within the nominal value ±0.5%. A similar $Al_{70}Z_{r30}$ capping layer was deposited on the top surface to protect the film from oxidation. Next, the sample was masked by using a conventional photolithographic technique. Local doping was realized by scanning a boron ion flux with an energy of 5 keV and an implantation dose of 2×10^{16} ions/cm^2, optimized according to simulations performed by using the stopping and range of ions in matter (SRIM) software [45–47]. The implantation along the surface of the masked sample resulted in regions, reproducing the mask, with nominal composition $Fe_{80}Zr_{10}B_{10}$, embedded in the $Fe_{89}Zr_{11}$ film. The implantation is always accompanied by some lateral diffusion of the ions. The lateral range was, however, estimated to be less than 10 nm for the implantation energy used. Finally, after chemically removing the mask, the sample consisted of a flat film with $Fe_{80}Zr_{10}B_{10}$ elements embedded in the $Fe_{89}Zr_{11}$ matrix.

Structural analysis using x-ray diffraction in grazing-incidence geometry, before and after implantation on an unmasked portion of the implanted sample, shows that both samples are amorphous, thus confirming that the implantation process did not induce any crystallization. X-ray reflectivity patterns were acquired and analyzed by using the GENX simulation software [48] to determine the thicknesses and roughness of the films. However, within the experimental uncertainties, it was not possible to detect any additional roughness or increment in the film thickness after the implantation. The boron implantation enhanced the Curie temperature T_C from approximately 208 K for $Fe_{89}Zr_{11}$ to approximately 340 K for $Fe_{80}Zr_{10}B_{10}$. The expected decrease in random magnetic anisotropy originating from a lower exchange frustration is manifested by a significant decrease in the coercivity seen in the $M(H)$ loops recorded at 5 K, from approximately 13 mT for $Fe_{89}Zr_{11}$ to approximately 0.2 mT for $Fe_{80}Zr_{10}B_{10}$ [49].

III. MAGNETIC PROPERTIES

A. Non-topographic ferromagnetic structures within a paramagnetic matrix

At RT, the structured films consist of non-topographically patterned FM $Fe_{80}Zr_{10}B_{10}$ elements embedded in the PM $Fe_{89}Zr_{11}$ matrix. Several composite films were prepared with magnetic patterns of different shapes; viz., stripes, sticks, triangles, and disks. All the shapes have a width of 20 μm and are placed in a regular square lattice with a center-to center distance of 40 μm. At this distance, we expect the dipolar coupling between the elements to be weak and the magnetic properties to depend mostly on the shape of the implanted elements. The $M(H)$ loops of all samples measured in different directions are shown in Fig. 2. The elongated structures, i.e., the stripes (20 μm × 4 mm) and the sticks (20 × 5 μm) exhibit strong shape anisotropy [Figs. 2(a) and 2(b), respectively]. It is interesting to observe that the magnetization reversal in the stripes occurs within an extremely narrow field range and in an almost single event. No sign of multi-domain formation was detected in the magneto-optic Kerr effect (MOKE) microscope images shown in Fig. 2(e), collected during $M(H)$ loop scans. The images were processed by using the software FIJI [50], normalizing the images brightness so as to have the same middle gray level for the paramagnetic background (matrix), allowing a better comparison of the brightness levels in different images. A

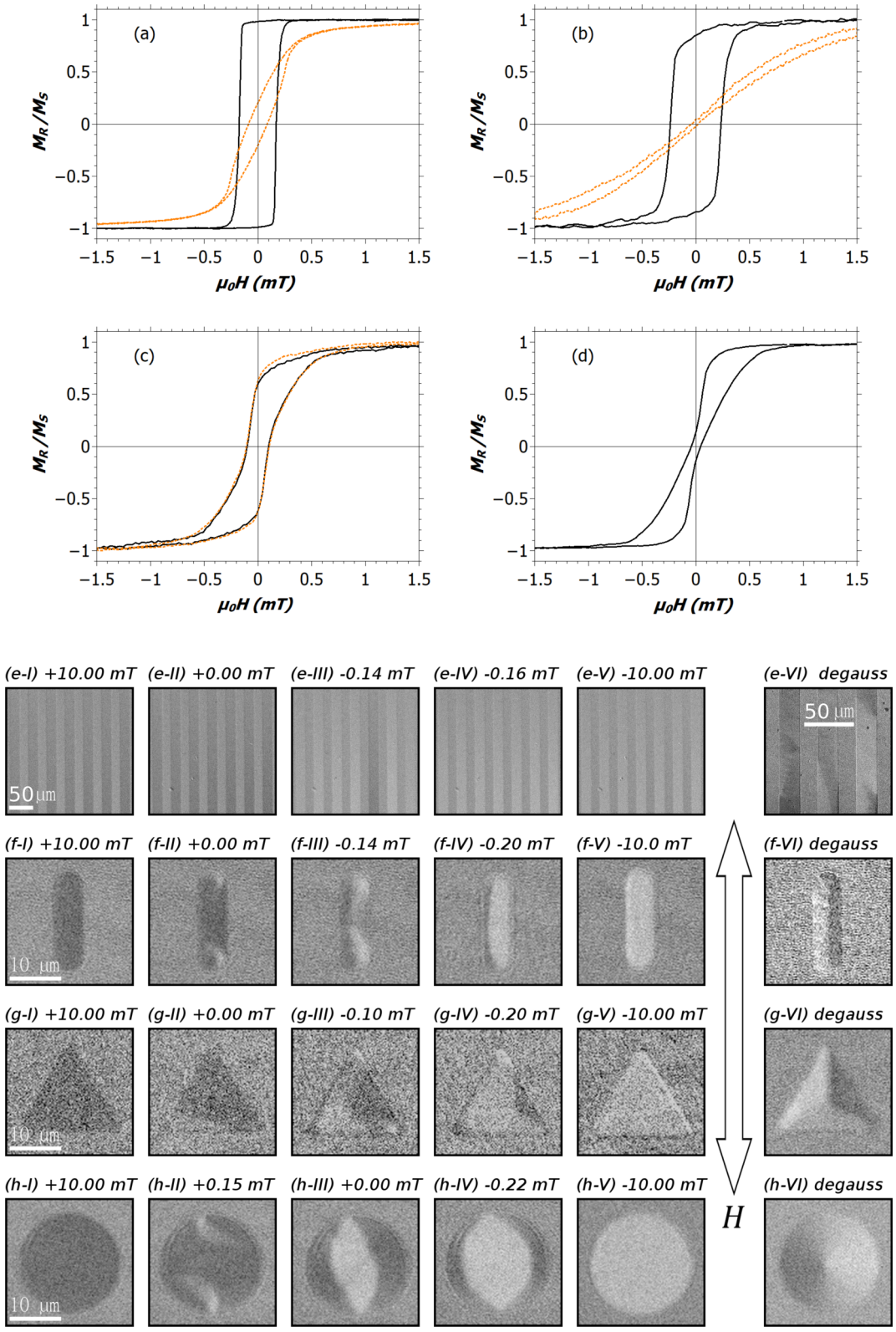

FIG. 2. Room-temperature $M(H)$ loop, measured using longitudinal MOKE at 300 K in a magnetic-field range of ± 6 mT, are here reported with a magnification in the range ± 1.5 mT, for (a) stripes, (b) sticks, (c) triangles, and (d) disks. The curves where measured with the field applied parallel (0°, black solid line) and perpendicular to the long edge (90°, orange dashed line) for the stripes and sticks, and perpendicular and parallel to the triangle bases. The domain configuration of the same samples was recorded by MOKE microscopy at 300 K. The images were collected during an $M(H)$ loop measured in a magnetic-field range of ± 10 mT, for (e) stripes, (f) sticks, (g) triangles, and (h) disks. The magnetic field was applied vertically with respect to the images, as indicated by the arrow. The panels on the right show the images recorded after a degauss process performed to reach the ground-state configuration.

multi-domain configuration was observed only after a degaussing process [Fig. 2(e)-VI]. The single-domain-like reversal of the 20-μm-wide and 4-mm-long stripes with the magnetic field applied along the easy axis is a sign of the isotropic soft magnetic properties of $Fe_{80}Zr_{10}B_{10}$ together with dominant shape anisotropy and it demonstrates the low concentration of defects acting as pinning centers for the magnetization reversal. During the magnetization reversal of the sticks, shown in Fig. 2(f), a double curling of the magnetization occurs. This is particularly visible at remanence and is related to the rounded shape of the endpoints of the sticks. In the triangles, the magnetization reversal, shown in Fig. 2(g), occurs via rotation of large domains in big steps. After degaussing, the ground state exhibits flux closure with a three-domain configuration [Fig. 2(g)-VI]. The shape of the $M(H)$ loops of the disk structures [shown in Fig. 2(d)] suggests the formation of vortices [51]. However, at remanence, a "diamond-like" configuration [52] with three antiparallel aligned domains is observed [Fig. 2(h)-III], while the statistics of the images collected after degaussing show that the most likely configuration (∼70% of approximately 50 analyzed disks) is, indeed, a vortex structure [Fig. 2(h)-VI]. The fact that a vortex is the ground state in a FM disc with such a large diameter (20 μm) can again be attributed to the soft and isotropic magnetic nature of $Fe_{80}Zr_{10}B_{10}$, and the low concentration of defects.

B. Ferromagnetic superstructures with long-range exchange coupling

Changing the temperature allows us to investigate how tuning the magnetic properties of the matrix affects the overall magnetic behavior of the superstructures. The FM $Fe_{80}Zr_{10}B_{10}$ elements are directly exchange coupled to the $Fe_{89}Zr_{11}$ matrix below its Curie temperature T_C^{matrix}, but the average exchange coupling is stronger within the B-implanted elements than in the matrix. With a FM matrix, we expect that the magnetic properties not only depend on the shape of the implanted elements, but also on their inter-distances. Therefore, we chose an elongated shape of the $Fe_{80}Zr_{10}B_{10}$ elements, the stick shape, with elements aligned vertically in patterns with different horizontal-vertical center-to-center distances between the sticks, namely, 40–40 μm, 25–25 μm, and 10–40 μm for the superstructures, labelled SS-A, SS-B, and SS-C, respectively. Microscope images of the masks used to create the three different superstructures are shown in Fig. 3, along with the temperature dependence of the coercivity measured along the long axis of the sticks for the three samples. The magnetic properties of the superstructures change significantly when the temperature is lowered below T_C^{matrix}, producing a sharp decrease in coercivity close to this temperature. $M(H)$ loops measured at different temperatures are also shown in Fig. 3. At temperatures above T_C^{matrix}, the shape of the sticks is the main source of anisotropy, and the magnetization reversal at 220 K is probably similar to that at RT, as described in Fig. 2. At temperatures below T_C^{matrix}, the $M(H)$ loops of the SS-A and SS-B samples exhibit a two-phase reversal with a "soft" component (the matrix) and a "hard" component (the implanted sticks) at all temperatures. For the SS-C sample, which has the shortest horizontal distance between the implanted $Fe_{80}Zr_{10}B_{10}$ elements, the *M(H)* curves exhibit a higher coercivity at low temperatures compared with the other samples. In particular, at 80 K, the $M(H)$ loop of the SS-C is almost square shaped, suggesting a single switching process in the sample due to a strong coupling between the "soft" and "hard" components.

To thoroughly investigate the magnetization-reversal mechanisms of all the samples at 80 K, we measured first-order reversal curves (FORCs) [53–56]. In a FORC measurement, the sample is saturated in a positive field, then the applied field is lowered to the reversal field H_r, and the FORC magnetization M is recorded as a function of the increasing measurement field H_m. Repeating the FORC measurement for different reversal fields H_r, the FORC distribution is obtained by computing the second-order mixed partial derivative of M with respect to H_m and H_r:

$$\rho(H_m, H_r) = \frac{-1}{2M_S} \frac{\partial^2 M(H_m, H_r)}{\partial H_m, \partial H_r}, \tag{1}$$

where M_S is the saturation magnetization. Depending on the H_r value, domains belonging to different parts of the sample are reversed away from the initial saturated condition. This allows us to identify different reversal and interaction mechanisms, since each back reversal event generates a specific signal in the FORC diagram. Due to the double derivative, only progressive changes of the $M(H_m, H_r)$ curves are visible in the ρ diagram. Thus, if a reversal event moves to a different H_m while increasing H_r, a new positive ρ signal will describe the new H_m value, while a negative one will be present at the corresponding previous H_m position creating a negative signal tail [57,58]. On the other hand, if a reversal event does not change H_m with respect to H_r, a positive signal will be visible in ρ only at the H_r at which the reversal is activated.

The FORC diagrams for the three samples at 80 K are shown in Fig. 4. SS-A and SS-B exhibit three different positive signals while SS-C exhibits only one positive signal, with a small tail. The origin of the three peaks in the ρ diagram are the same for SS-A [Fig. 4(a)] and SS-B [Fig. 4(b)]; the peak labeled *I* at the lowest H_r corresponds to only the matrix being reversed by H_r and being back-reversed by H_m. The second peak, labeled *II*, corresponds to both components, the matrix and the implanted sticks, being reversed by the reversal field and it is produced by the matrix being back-reversed at a higher H_m under the influence of the reversed sticks. The third peak, labeled *III*, corresponds to the back-reversal of the implanted regions. This third peak is stronger in SS-B than in SS-A because of the higher fraction of B-implanted sticks. The center-to-center horizontal distance of 10 μm between the implanted regions in sample SS-C [Fig. 4(c)] is short enough to produce long-range exchange coupling between the soft and the hard phases, with a single peak in ρ and the coercivity shifted towards the value of the hard phase. Strong exchange coupling is usually manifested only by nanostructured materials [59]. Goto *et al.* [60] introduced a model for the interfacial exchange-spring coupling between a soft and hard phase. According to this conventional model, the soft phase is parallel to the hard phase as long as an external opposite field does not exceed the magnitude of the exchange field H_{ex}, which quantifies the interphase coupling. If the reversal field of the hard phase H_r^{hard} is smaller than H_{ex}, the two phases can reverse coherently as a single component. The critical thickness t_s^{crit} for a rigidly

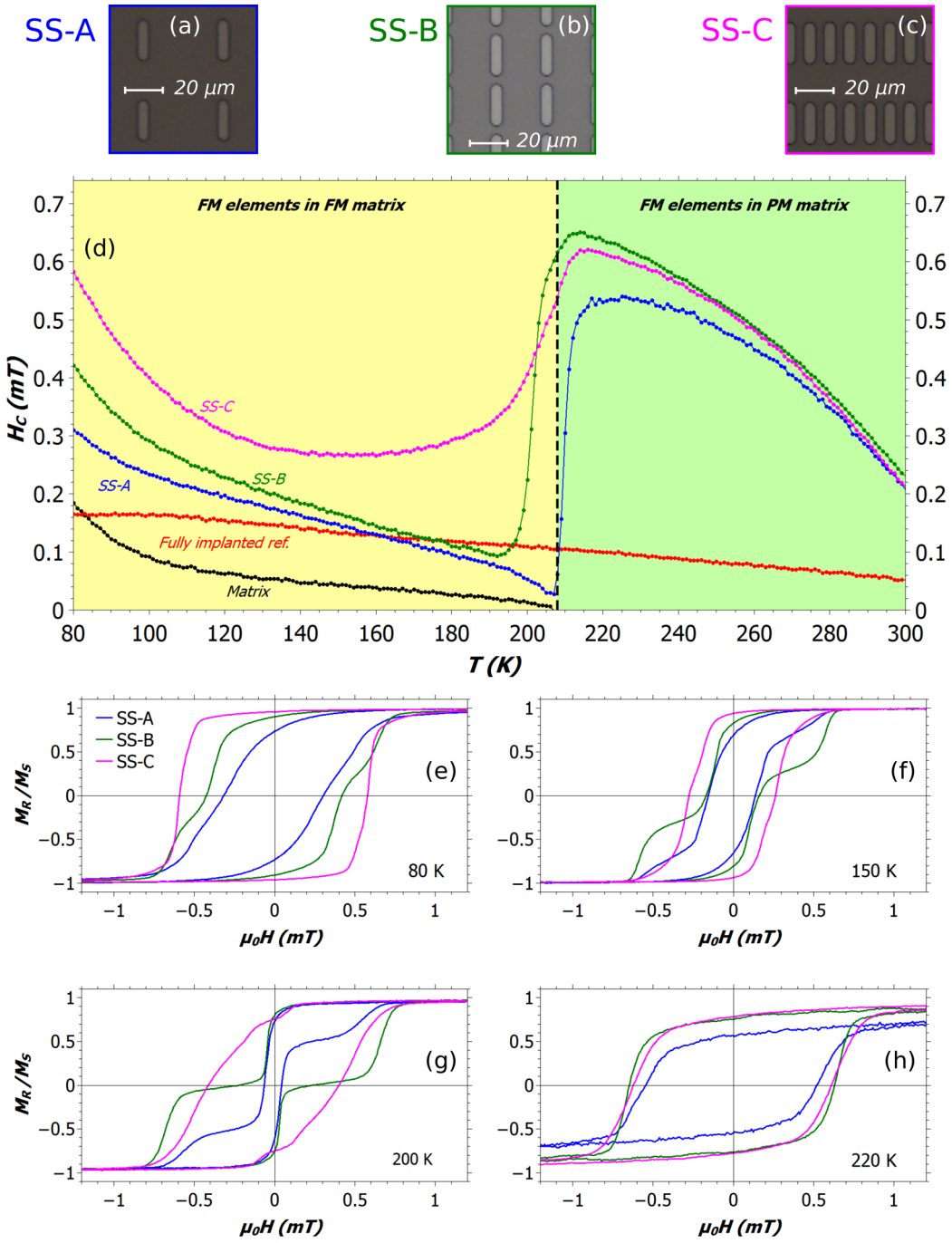

FIG. 3. Microscopy images of samples (a) SS-A, (b) SS-B, and (c) SS-C before removing the mask used for the implantation. Panel (d) shows the thermal dependence of the coercivity of the superstructures, the original matrix, and a fully implanted sample. The dashed vertical black line marks the Curie temperature of the matrix (∼208 K). The $M(H)$ loops of the superstructures measured at 80, 120, 180, and 200 K are exhibited in panels (e), (f), (g), and (h), respectively. The $M(H)$ loops were measured by L-MOKE with the magnetic field applied along the long edge of the sticks.

exchange coupled system is given by

$$t_s^{\text{crit}} = \sqrt{\frac{\pi^2 A_{\text{soft}}}{2M_S^{\text{soft}}\mu_0 H_r^{\text{hard}}}}. \tag{2}$$

We have estimated the exchange stiffness of the matrix $A_{\text{soft}} = 4(2) \times 10^{-12}\,\text{J/m}$, according to the values reported in the literature for amorphous iron zirconium alloys with similar T_C [61–63], yielding $t_s^{\text{crit}} = 200(50)\,\text{nm}$. This value is too small to explain the rigid exchange coupling observed in SS-C with the conventional model of Goto *et al.* We need to remember that the ion-implantation modulates the atomic exchange coupling without introducing structural interfaces, and that the lateral diffusion of implanted ions, despite being restricted to a few nanometers, gives a smooth and gradual variation in chemical composition and hence of the atomic

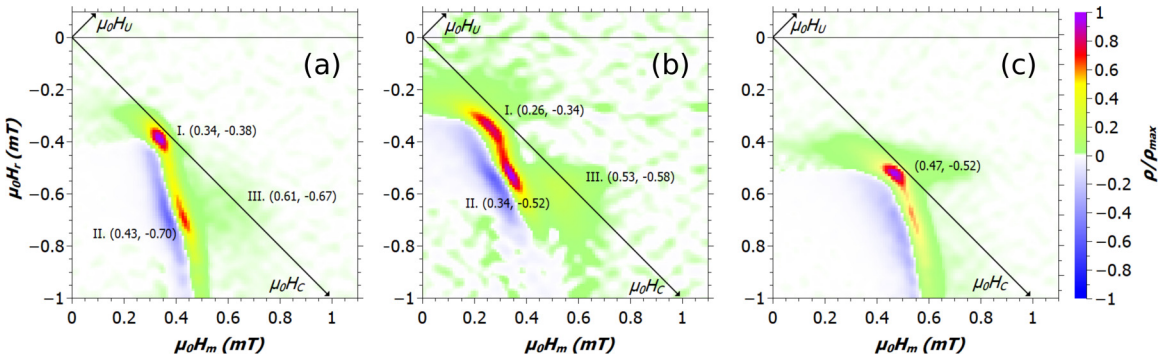

FIG. 4. FORC distributions calculated from the data measured at 80 K for (a) SS-A, (b) SS-B, and (c) SS-C with a L-MOKE setup. As a reference, the translated coordinates $H_C = (H_m - H_r)/2$, and $H_U = (H_m + H_r)/2$ are also reported. The main reversal processes are evidenced reporting the field coordinates of the events.

exchange coupling between implanted and pristine regions. Due to the absence of conventional interfaces, nothing forces the presence of inter-phase domain walls, thus allowing for long-range exchange interactions, which could produce large domains. We note that giant domains have already been observed in single-phase amorphous alloys [64]. An additional novel aspect in the all amorphous superstructure is the nature of the hard-phase anisotropy. While conventionally the hard phase exhibits strong magneto-crystalline anisotropy [65], here the intrinsic anisotropy of the implanted regions is weaker than that of the original matrix, and the main source of anisotropy is the elongated shape of the implanted element. This symmetry affects also the symmetry of the coupling. Indeed, both SS-A and SS-C have the same vertical distance among sticks, but only when the horizontal separation is reduced in SS-C, a strong exchange coupling emerges.

This approach to exchange coupling two similar amorphous phases opens a pathway for designing magnetic materials with tunable anisotropy. The use of elongated shapes and the reduction of the size of the patterns down to the nanoscale, would allow tuning of the shape anisotropy and, thereby, of the coercivity. Furthermore, using, e.g., amorphous $Co_{100-x-y}Fe_xZr_y$ as a matrix, the T_C^{matrix} can be tuned by the Co content up to well above RT. Other amorphous materials such as $Co_{100-x}Sm_x$, for which large magnetic domains have been reported [64], could also be an interesting matrix material. For the ion implantation, one is counter-intuitively searching for dopants that can reduce the intrinsic anisotropy and enhance the exchange interaction, while the magnetic hardness of the implanted region, produced by the shape, is tunable both in magnitude and symmetry.

IV. CONCLUSION

In summary, we have proposed superstructures consisting of two structurally similar amorphous materials as a route to create artificial magnetic systems with emergent properties. A spatial variation of the chemical composition, and hence of the physical properties, has been realized by ion implantation through a mask. The lack of crystalline interfaces and the associated defects makes it possible to create well-defined elements with smooth interfaces. In the investigated model superstructures, consisting at room temperature of FM $Fe_{80}Zr_{10}B_{10}$ elements embedded in a PM $Fe_{89}Zr_{11}$ matrix, a low concentration of defects acting as pinning centers for the magnetization reversal has been evidenced by a vortex ground state in FM disks with a diameter of 20 μm as well as by single-domain-like reversal in 20-μm-wide FM stripes. Using temperature as a parameter to tune the magnetic properties of the matrix, superstructures consisting of FM B-implanted elements in a FM matrix were investigated at low temperatures. Due to an elongated shape of the implanted elements, they make up a hard-phase in a soft matrix, and by reducing the distance between the implanted elements, from 35 to 5 μm, a strong exchange coupling between the "hard" and the "soft" phase is obtained, resulting in a single-phase reversal of the magnetization as evidenced by FORC measurements. This constitutes an experimental observation of a rigid exchange coupled two-phase system with microscale dimensionality. An intuitive model for the interphase exchange coupling is provided, where the key points are the absence of sharp structural interfaces, and the coercivity of the hard phase created and tailored both in magnitude and symmetry only by the shape of the implanted elements. This work represents a proof of concept of the all-amorphous design of magnetic superstructures. It can be extended to different amorphous materials and patterning tools, making it possible to realize structures of nanosize. The design can also be extended to create complex three-dimensional embedded elements by using multi-layered films as matrix. The results open new perspectives for exploring the physics of all-amorphous nano- and microstructures and for tuning their properties to suit applications.

ACKNOWLEDGMENTS

We acknowledge financial support from the Swedish Research Council (VR). The authors thank Carl-Johan Fridén and Anders Hallén for the ion implantation process, and Daniel Primetzhofer for performing the RBS measurements. The authors also thank Tapati Sarkar and Venkata Kamalakar Mutta for proofreading the manuscript, Heikki Palonen for useful discussions, and Gabriella Andersson for helping with the MOKE microscope.

[1] U. G. K. Wegst, H. Bai, E. Saiz, A. P. Tomsia, and R. O. Ritchie, Nat. Mater. **14**, 23 (2014).

[2] A. Llordés, G. Garcia, J. Gazquez, and D. J. Milliron, Nature (London) **500**, 323 (2013).

[3] S. Kim, J. Byun, S. Choi, D. Kim, T. Kim, S. Chung, and Y. Hong, Adv. Mater. **26**, 3094 (2014).

[4] C. A. F. Vaz, J. Hoffman, C. H. Ahn, and R. Ramesh, Adv. Mater. **22**, 2900 (2010).

[5] Q. Cheng, J. Duan, Q. Zhang, and L. Jiang, ACS Nano **9**, 2231 (2015).

[6] G. Muscas, P. Anil Kumar, G. Barucca, G. Concas, G. Varvaro, R. Mathieu, and D. Peddis, Nanoscale **8**, 2081 (2016).

[7] X. Xia, D. Chao, Z. Fan, C. Guan, X. Cao, H. Zhang, and H. J. Fan, Nano Lett. **14**, 1651 (2014).

[8] H. D. Wagner and R. A. Vaia, Mater. Today **7**, 38 (2004).

[9] J. L. MacManus-Driscoll, Adv. Funct. Mater. **20**, 2035 (2010).

[10] M. V. Gorkunov, S. A. Gredeskul, I. V. Shadrivov, and Y. S. Kivshar, Phys. Rev. E **73**, 056605 (2006).

[11] L. Wu, J. J. Willis, I. S. McKay, B. T. Diroll, J. Qin, M. Cargnello, and C. J. Tassone, Nature (London) **548**, 197 (2017).

[12] E. Josten, E. Wetterskog, A. Glavic, P. Boesecke, A. Feoktystov, E. Brauweiler-Reuters, U. Rücker, G. Salazar-Alvarez, T. Brückel, and L. Bergström, Sci. Rep. **7**, 2802 (2017).

[13] Z. Zhang, P. Chen, X. Duan, K. Zang, J. Luo, and X. Duan, Science **357**, 788 (2017).

[14] K. Kang, K.-H. Lee, Y. Han, H. Gao, S. Xie, D. A. Muller, and J. Park, Nature (London) **550**, 229 (2017).

[15] I. J. Beyerlein, M. J. Demkowicz, A. Misra, and B. P. Uberuaga, Prog. Mater. Sci. **74**, 125 (2015).

[16] B. Dai, T. Kato, S. Iwata, and S. Tsunashima, IEEE Trans. Magn. **48**, 3223 (2012).

[17] D. Kim, K. Y. Jung, S. Joo, Y. Jang, J. Hong, B. C. Lee, C. Y. You, J. H. Cho, M. Y. Kim, and K. Rhie, J. Magn. Magn. Mater. **374**, 350 (2015).

[18] K. I. Jun, J. H. Lee, K. H. Shin, K. Rhie, and B. C. Lee, J. Magn. Magn. Mater. **286**, 158 (2005).

[19] F. Magnus, M. E. Brooks-Bartlett, R. Moubah, R. A. Procter, G. Andersson, T. P. A. Hase, S. T. Banks, and B. Hjörvarsson, Nat. Commun. **7**, 11931 (2016).

[20] M. Ahlberg, G. Andersson, and B. Hjörvarsson, Phys. Rev. B **83**, 224404 (2011).

[21] M. Ahlberg, A. Zamani, E. Östman, H. Fashandi, B. Hjörvarsson, and P. E. Jönsson, Phys. Rev. B **90**, 184403 (2014).

[22] Y.-Y. Zhao, A. Inoue, C. Chang, J. Liu, B. Shen, X. Wang, and R.-W. Li, Sci. Rep. **4**, 5733 (2015).

[23] A. Inoue, T. Zhang, and A. Takeuchi, Appl. Phys. Lett. **71**, 464 (1997).

[24] P. Sharma, H. Kimura, and A. Inoue, Phys. Rev. B **78**, 134414 (2008).

[25] C. Chappert, H. Bernas, J. Ferre´, V. Kottler, J.-P. Jamet, Y. Chen, E. Cambril, T. Devolder, F. Rousseaux, V. Mathet, and H. Launois, Science **280**, 1919 (1998).

[26] J. Fassbender and J. McCord, J. Magn. Magn. Mater. **320**, 579 (2008).

[27] M. Jaafar, R. Sanz, J. McCord, J. Jensen, R. Schäfer, M. Vázquez, and A. Asenjo, Phys. Rev. B **83**, 094422 (2011).

[28] A. Varea, E. Menéndez, J. Montserrat, E. Lora-Tamayo, A. Weber, L. J. Heyderman, S. C. Deevi, K. V. Rao, S. Suriñach, M. D. Baró, K. S. Buchanan, J. Nogués, J. Sort, E. Menéndez, J. Montserrat, E. Lora-Tamayo, A. Weber, L. J. Heyderman, S. C. Deevi, K. V. Rao, S. Suriñach, M. D. Baró;, K. S. Buchanan, J. Nogués, and J. Sort, J. Appl. Phys. **109**, 093918 (2011).

[29] T. Mewes, R. Lopusnik, J. Fassbender, B. Hillebrands, M. Jung, D. Engel, A. Ehresmann, and H. Schmoranzer, Appl. Phys. Lett. **76**, 1057 (2000).

[30] D. McGrouther and J. N. Chapman, Appl. Phys. Lett. **87**, 022507 (2005).

[31] T. Devolder, I. Barisic, S. Eimer, K. Garcia, J.-P. Adam, B. Ockert, and D. Ravelosona, J. Appl. Phys. **113**, 203912 (2013).

[32] N. Martin, J. McCord, A. Gerber, T. Strache, T. Gemming, I. Mönch, N. Farag, R. Schäfer, J. Fassbender, E. Quandt, and L. Schultz, Appl. Phys. Lett. **94**, 062506 (2009).

[33] C. Surgers, K. Potzger, T. Strache, W. Möller, G. Fischer, N. Joshi, H. v. Löhneysen, C. Sürgers, K. Potzger, T. Strache, W. Möller, G. Fischer, N. Joshi, and H. V. Löhneysen, Appl. Phys. Lett. **93**, 062503 (2008).

[34] E. Menéndez, M. O. Liedke, J. Fassbender, T. Gemming, A. Weber, L. J. Heyderman, K. V. Rao, S. C. Deevi, S. Suriñach, M. D. Baró, J. Sort, and J. Nogués, Small **5**, 229 (2009).

[35] S. Kim, S. Lee, J. Ko, J. Son, M. Kim, S. Kang, and J. Hong, Nat. Nanotechnol. **7**, 567 (2012).

[36] S. Kim, S. Lee, and J. Hong, ACS Nano **8**, 4698 (2014).

[37] H. Ren and D. H. Ryan, Phys. Rev. B **51**, 15885 (1995).

[38] A. Zamani, R. Moubah, M. Ahlberg, H. Stopfel, U. B. Arnalds, A. Hallén, B. Hjörvarsson, G. Andersson, and P. E. Jönsson, J. Appl. Phys. **117**, 143903 (2015).

[39] S. Bao-gen, X. Rufeng, Z. Jian-gao, and Z. Wen-shan, Phys. Rev. B **43**, 11005 (1991).

[40] R. Moubah, A. Zamani, A. Olsson, S. Shi, A. Hallén, S. Carlson, D. Arvanitis, P. Nordblad, B. Hjörvarsson, and P. Jönsson, Appl. Phys. Express **6**, 053001 (2013).

[41] J. M. Barandiaran, P. Gorria, J. C. Gomez Sal, L. Fernandez Barquin, and S. N. Kaul, IEEE Trans. Magn. **30**, 4776 (1994).

[42] K. A. Gallagher, M. A. Willard, V. N. Zabenkin, D. E. Laughlin, and M. E. McHenry, J. Appl. Phys. **85**, 5130 (1999).

[43] P. T. Korelis, A. Liebig, M. Björck, B. Hjörvarsson, H. Lidbaum, K. Leifer, and A. R. Wildes, Thin Solid Films **519**, 404 (2010).

[44] M. Mayer, AIP Conf. Proc. **475**, 541 (1999).

[45] J. F. Ziegler, M. D. Ziegler, and J. P. Biersack, Nucl. Instruments Methods Phys. Res. Sect. B Beam Interact. Mater. Atoms **268**, 1818 (2010).

[46] J. P. Biersack and J. F. Ziegler, in *Ion Implant. Tech. Springer Ser. Electrophysics* (1982), Vol. 10, pp. 122–156.

[47] See Supplemental Material at http://link.aps.org/supplemental/10.1103/PhysRevB.97.174409 for a full description of the sample preparation and the implantation simulation.

[48] M. Björck and G. Andersson, J. Appl. Crystallogr. **40**, 1174 (2007).

[49] See Supplemental Material at http://link.aps.org/supplemental/10.1103/PhysRevB.97.174409 for the experimental data on the structural and magnetic properties of the samples before and after implantation.

[50] J. Schindelin, I. Arganda-Carreras, E. Frise, V. Kaynig, M. Longair, T. Pietzsch, S. Preibisch, C. Rueden, S. Saalfeld, B. Schmid, J.-Y. Tinevez, D. J. White, V. Hartenstein, K. Eliceiri, P. Tomancak, and A. Cardona, Nat Meth **9**, 676 (2012).

[51] M. Getzlaff, *Fundamentals of Magnetism* (Springer, Berlin, Heidelberg, 2008).

[52] C. A. F. Vaz, M. Kläui, L. J. Heyderman, C. David, F. Nolting, and J. A. C. Bland, Phys. Rev. B **72**, 224426 (2005).

[53] C. R. Pike, Phys. Rev. B **68**, 104424 (2003).
[54] C. I. Dobrotă and A. Stancu, J. Appl. Phys. **113**, 043928 (2013).
[55] D. A. Gilbert, J. W. Liao, L. W. Wang, J. W. Lau, T. J. Klemmer, J. U. Thiele, C. H. Lai, and K. Liu, APL Mater. **2**, 086106 (2014).
[56] S. Ruta, O. Hovorka, P.-W. Huang, K. Wang, G. Ju, and R. Chantrell, Sci. Rep. **7**, 45218 (2017).
[57] D. A. Gilbert, G. T. Zimanyi, R. K. Dumas, M. Winklhofer, A. Gomez, N. Eibagi, J. L. Vicent, and K. Liu, Sci. Rep. **4**, 4204 (2015).
[58] D. A. Gilbert, L. Ye, A. Varea, S. Agramunt-Puig, N. del Valle, C. Navau, J. F. López-Barbera, K. S. Buchanan, A. Hoffmann, A. Sánchez, J. Sort, K. Liu, and J. Nogués, Nanoscale **7**, 9878 (2015).
[59] A. López-Ortega, M. Estrader, G. Salazar-Alvarez, A. G. Roca, and J. Nogués, Phys. Rep. **553**, 1 (2015).
[60] E. Goto, N. Hayashi, T. Miyashita, and K. Nakagawa, J. Appl. Phys. **36**, 2951 (1965).
[61] L. F. Kiss, T. Kemény, J. Bednarčík, J. Gamcová, and H.-P. Liermann, Phys. Rev. B **93**, 214424 (2016).
[62] M. W. Grinstaff, M. B. Salamon, and K. S. Suslick, Phys. Rev. B **48**, 269 (1993).
[63] X. Y. Xiong, B. C. Muddle, and T. R. Finlayson, J. Phys. D.: Appl. Phys. **36**, 223 (2003).
[64] F. Magnus, R. Moubah, U. B. Arnalds, V. Kapaklis, A. Brunner, R. Schäfer, G. Andersson, and B. Hjörvarsson, Phys. Rev. B **89**, 224420 (2014).
[65] F. Liu, Y. Hou, and S. Gao, Chem. Soc. Rev. **43**, 8098 (2014).